Journal of Solid State Chemistry 183 (2010) 1529–1535

Contents lists available at ScienceDirect

Journal of Solid State Chemistry

journal homepage: www.elsevier.com/locate/jssc

Crystal structure and physical properties of the quaternary manganese-bearing pavonite homologue $Mn_{1.34}Sn_{6.66}Bi_8Se_{20}$

Clarence Anglin, Nathan Takas, Juan Callejas, Pierre F.P. Poudeu *

The Advanced Materials Research Institute and Department of Chemistry, University of New Orleans, New Orleans, LA 70148, USA

ARTICLE INFO

Article history:
Received 3 February 2010
Received in revised form
16 April 2010
Accepted 25 April 2010
Available online 13 May 2010

Keywords:
Bismuth selenide
Manganese
Tin
Thermoelectricity
Magnetism
Semiconductor

ABSTRACT

The quaternary manganese tin bismuth selenide, $Mn_{1.34}Sn_{6.66}Bi_8Se_{20}$ was synthesized by combining constituent elements at 723 K. Single crystal structure determination revealed that $Mn_{1.34}Sn_{6.66}Bi_8Se_{20}$ is isostructural to the mineral pavonite, $AgBi_3S_5$, crystallizing in the monoclinic space group $C2/m$ (#12) with $a=13.648(3)$ Å; $b=4.175(1)$ Å; $c=17.463(4)$ Å; $\beta=93.42(3)^\circ$. In the structure, two kinds of layered modules, denoted A and B, alternate along [0 0 1]. Module A consists of paired chains of face-sharing monocapped trigonal prisms (around Bi/Sn) separated by a single chain of edge-sharing octahedra (around Mn/Sn). Module B represents a NaCl-type fragment of edge-sharing [(Bi/Sn)Se_6] octahedra. $Mn_{1.34}Sn_{6.66}Bi_8Se_{20}$ is an n-type narrow gap semiconductor with $E_g \sim 0.29$ eV. At 300 K, thermopower, electrical conductivity and lattice thermal conductivity values are -123 μV/K, 47 S/cm and 0.6 W/m K, respectively. $Mn_{1.34}Sn_{6.66}Bi_8Se_{20}$ is paramagnetic at high temperatures and undergoes antiferromagnetic transition at $T_N=10$ K.

1. Introduction

Multinary complex chalcogenides with low-dimensional magnetic substructures are currently the target of widespread investigation. Interest in this family of compounds derives from peculiar physical properties which are generally associated with low dimensional structures. Additionally, the flexibility of their framework structures opens tremendous avenues to create within a single structure, materials with multiple functionalities through careful manipulation of the composition at targeted atomic positions. For instance, the "natural" complex iron and manganese sulfides MSb_2S_4 (M=Mn, Fe) [1,2] and $MPb_4Sb_6S_{14}$ (M=Fe, Mn) [1,3–7] were investigated for their magnetic and thermoelectric properties. All of these compounds feature isolated single chains of iron or manganese atoms in octahedral coordination. Spiral magnetic structures were observed in MSb_2S_4 (M=Fe, Mn) with antiferromagnetic interactions between identical chains in $FeSb_2S_4$ (berthierite), whereas ferromagnetic interactions were observed in the Mn analog [1,2]. The $MPb_4Sb_6S_{14}$ (M=Fe, Mn) phases showed antiferromagnetic ordering below 30 K and neutron diffraction investigations of the magnetic structures indicated that $FePb_4Sb_6S_{14}$ (Jamesonite) is a canted antiferromagnet, while no canting angle was detected in the Mn analog (Benavidesite) [1]. In addition to the observed interesting magnetic properties, $FePb_4Sb_6S_{14}$ (Jamesonite) was found to exhibit semiconducting behavior with narrow energy gap ($E_g=0.48$ eV) and large thermopower value (~ -200 μV/K at 300 K) [8]. Recently, we have embarked in the development of new physicochemical concepts to design multifunctional inorganic materials combining low-dimensional magnetic substructures with semiconducting three-dimensional frameworks. Our approach has been centered on the integration of magnetic transition metal atoms into selected metal positions in "natural" and "synthetic" multinary chalcogenides in anticipation of new magneto-electric phenomena that may arise from the low dimensionality of the magnetic substructure and the local environments of the transition metals. In this context, we recently described the quaternary transition metal chalcogenides $Fe_xPb_{4-x}Sb_4Se_{10}$ ($0 \le x \le 2$) [9], and $MnSn_3Bi_8Q_{16}$ (Q=S, Se) [10]. $Fe_xPb_{4-x}Sb_4Se_{10}$ ($0 \le x \le 2$) phases feature quasi-one-dimensional double-chains of edge-sharing $\{Fe_2Se_{10}\}$ octahedra separated by semiconducting inorganic framework of corrugated layers of edge-sharing bicapped trigonal prisms and octahedra interconnected by NaCl-type {SbSe} ribbons. $Fe_xPb_{4-x}Sb_4Se_{10}$ ($0 \le x \le 2$) phases are ferromagnetic at and below 300 K and exhibit superparamagnetism at higher temperatures. $MnSn_3Bi_8Q_{16}$ (Q=S, Se) belong to the pavonite homologous series $M_{N+1}Bi_2S_{N+5}$ (M=Cu, Ag, Sn, Pb, Bi), which is found for minerals in the Ag_2S–PbS–Bi_2S_3 system [11–19]. The pavonite structures consist of two types of building units alternating along the c-axis. The first building unit denoted A, which is similar in all members of the series, is built of chains of paired monocapped trigonal prisms separated by a single chain of edge-sharing octahedra. Members of the pavonite series are differentiated by the second building unit denoted B, which is essentially a NaCl-type fragment with thickness defined by the number (N) of edge-sharing octahedra along its central

* Corresponding author. Fax: +1 504 280 3185.
E-mail address: ppoudeup@uno.edu (P.F.P. Poudeu).

0022-4596/$ - see front matter © 2010 Elsevier Inc. All rights reserved.
doi:10.1016/j.jssc.2010.04.035

diagonal. In the structure of known pavonite members within the Ag_2S–PbS–Bi_2S_3 system, the octahedral metal position in unit A is exclusively occupied by the monovalent atom Ag, while the monocapped trigonal prism is fully occupied by Bi. Octahedral metal positions within building unit B show mixed occupancy between Pb and Bi. $MnSn_3Bi_8Q_{16}$ (Q=S, Se), which are members with N=3 of the pavonite series, displayed mixing between Sn and Mn in the octahedral metal position within building unit A to form a quasi-one dimensional magnetic chains of edge-sharing octahedra running along [0 1 0], while the remaining metal positions are mixed occupied by Bi and Sn. $MnSn_3Bi_8Se_{16}$ showed antiferromagnetic ordering below 20 K where Mn takes a 2+ oxidation state. Electronic charge transport measurements revealed that $MnSn_3Bi_8Se_{16}$ is an n-type semiconductor with room temperature values of the thermopower, electrical conductivity and lattice thermal conductivity of −98 μV/K, 133 S/cm and ~0.7 W/m K, respectively. Here, we report the crystal structure, magnetic and thermoelectric properties of $Mn_{1.34}Sn_{6.66}Bi_8Se_{20}$, a new member of the pavonite series (N=5) in the Mn–Sn–Bi–Se system. We demonstrate that the substitution of monovalent Ag atom by the bivalent Mn atom in the pavonite structure generates a redistribution of atoms within all metal positions. The redistribution of atoms within the structural framework could present opportunities to systematically modify physical properties by isostructural modification of the composition [20]. $Mn_{1.34}Sn_{6.66}Bi_8Se_{20}$ shows antiferromagnetic ordering below 10 K and exhibits n-type semiconducting behavior with a remarkably low lattice thermal conductivity of ~0.6 W/m K at 300 K.

2. Experimental

2.1. Synthesis

Single crystals of $Mn_{1.34}Sn_{6.66}Bi_8Se_{20}$ were first obtained as byproduct of a reaction designed to prepare polycrystalline powder of $Mn_2Sn_2Bi_8Se_{16}$, a composition isostructural to $MnSn_3Bi_8Se_{16}$ [10] in which isolated one-dimensional chains of edge-sharing {$MnSe_6$} octahedra are expected. Polycrystalline single phase powder of $Mn_{1.34}Sn_{6.66}Bi_8Se_{20}$ was later synthesized using Mn metal powder (CERAC, 99.8%), Sn metal powder (CERAC, 99.8%), Bi metal pieces (Aldrich, 99.999%) and Se powder (CERAC, 99.999%) as starting materials. All four components weighed in the desired ratio (total mass=5 g) under argon atmosphere in a dry glove box, were thoroughly mixed in an agate mortar with pestle and transferred into a fused silica tube ($\varnothing_{ID}$=7 mm, length=20 cm). The tube was flame-sealed under residual pressure of ~10^{-4} Torr. The sealed tube was then inserted into a mullite casing and isolated using ceramic fibers. This precaution is necessary to minimize the temperature gradient inside the quartz tube during the reaction. The protected-tube was then placed into a tube furnace and the temperature was raised to 623 K in 12 h, dwelled for 24 h and finally increased to 773 K. 72 h dwelling at 773 K was necessary to complete the reaction. The furnace was then slowly cooled to room temperature over 80 h. The resulting product was dark gray polycrystalline powder containing small black needle-shape crystals of $Mn_{1.34}Sn_{6.66}Bi_8Se_{20}$. The synthesized air-stable polycrystalline powder of $Mn_{1.34}Sn_{6.66}Bi_8Se_{20}$ was finely ground in an agate mortar with pestle and used for further characterization. Approximately 3 g of the material was used for the fabrication of a high density pellet for thermoelectric properties measurements. An approximately 96% dense pellet of $Mn_{1.34}Sn_{6.66}Bi_8Se_{20}$ was obtained using a uniaxial hot press from Thermal Technologies Inc. The pressing was carried out under dynamic vacuum (~10^{-4} Torr) at 673 K using an applied pressure of 100 MPa. The resulting disk-shaped pellet with approximate thickness of 3 mm and diameter of 13 mm was then polished for thermal diffusivity measurements. A rectangular bar specimen, with approximate dimensions 2.5 × 2.5 × 10 mm^3 was cut from the pressed pellet using a precision wire saw (South Bay Technology) and used for simultaneous measurement of the electrical conductivity and thermopower. All faces of the rectangular bar were polished to a mirror-like finish with SiC sandpaper and washed with ethanol and acetone to remove any remaining particles from the surface before measurements.

2.2. Characterization

2.2.1. X-ray powder diffraction

The X-ray diffraction pattern of finely ground $Mn_{1.34}Sn_{6.66}Bi_8Se_{20}$ powder was collected using Cu–$K\alpha$ radiation (λ=1.54056 Å) in reflection geometry on a PANalytical X-ray powder diffractometer with position sensitive detector and operating at 45 kV and 40 mA. To assess the phase purity of the sample, the experimental X-ray diffraction pattern of $Mn_{1.34}Sn_{6.66}Bi_8Se_{20}$ was compared to the theoretical pattern calculated from the single crystal structure data using PowderCell [21]. The observed good agreement between both patterns (Fig. 1) indicates that nearly single phase (95% to 97% purity) of $Mn_{1.34}Sn_{6.66}Bi_8Se_{20}$ was successfully synthesized via solid state combination of the constituents. Trace amount (3% to 5%) of Bi_2Se_3 could also be detected in the experimental pattern.

2.2.2. Single crystal structure determination

A needle shaped single crystal of $Mn_{1.34}Sn_{6.66}Bi_8Se_{20}$ with approximate dimensions 0.03 × 0.06 × 0.1 mm^3 was mounted on the tip of a glass fiber using a two-component epoxy glue. The intensity data were recorded at 299 K on a IPDS-2 T diffractometer from STOE using graphite-monochromated Mo$K\alpha$ radiation (λ=0.71073 Å) and the Stoe-X-area [22] software package for data acquisition, integration, reduction and absorption correction. Intensity data were best indexed in the monoclinic crystal system, space group $C2/m$ (#12), with a=13.648(3) Å; b=4.463(8) Å; c=17.463(4) Å; β=93.42(3)° and the structure was solved and refined using the SHELTXL package [23]. Ten crystallographically

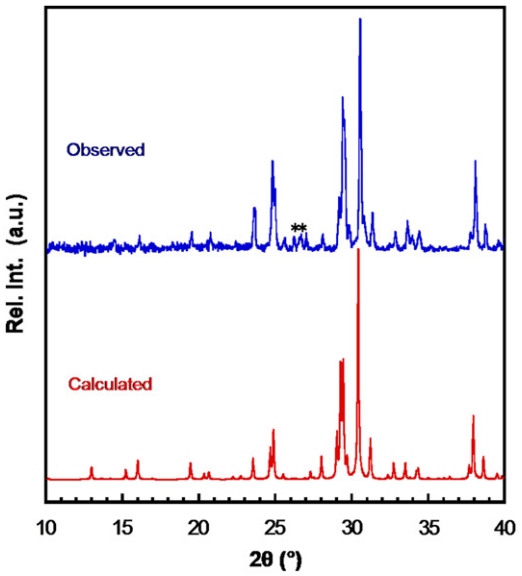

Fig. 1. (A) X-ray powder diffraction pattern of $Mn_{1.34}Sn_{6.66}Bi_8Se_{20}$ compared with the theoretical pattern calculated from the crystal structure refinement data. Peaks corresponding to Bi_2Se_3 are indicated with *.

independent positions (Bi 1–4, Mn1, Se 1– 5) were located on mirror planes ($y=0$ and 1/2). The refinement of this model yielded a high agreement factor of $R_1 \sim 23\%$ and unusually large thermal displacement parameters were observed for the Bi 1–4 sites. In addition, the Mn1 position also showed a small thermal displacement parameter. We therefore introduced a disorder model with Bi/Sn mixed occupancies at Bi 1–4 sites and Mn/Sn mixed occupancy at Mn site. Each mixed position was constrained to full occupancy and a restraint for electroneutrality of the compound was included. The refinement resulted in more acceptable thermal displacement parameters for all atoms. In the final refinement cycles secondary extinction corrections and anisotropic displacement parameters for all atoms were included. This resulted in the R_1 and wR_2 values dropping to 2.1% and 5.7%, respectively. Assuming Mn^{2+}, Sn^{2+}, Bi^{3+} and Se^{2-}, the composition of the crystal was freely refined to the charge balanced formula $Mn_{1.34(2)}Sn_{6.66(2)}Bi_{7.98(2)}Se_{20}$ with 48% Sn on Bi1, 43% Sn on Bi2, 30%Sn on Bi3, 59% Sn on Bi4 and 33%Sn on Mn1 positions. The refined composition is in agreement with composition of the crystal, $Mn_{1.3(4)}Sn_{7.2(5)}Bi_{8.3(6)}Se_{19.7(7)}$ obtained by energy dispersive X-ray analysis (EDX). Selected crystallographic data for $Mn_{1.34}Sn_{6.66}Bi_8Se_{20}$ are given in Table 1. The atomic coordinates, site occupancies and isotropic displacement parameters of all atoms are given in Table 2 and selected interatomic distances are shown in Table 3. Further details of the crystal structure investigation can be obtained from the Fachinformationszentrum Karlsruhe, 76344 Eggenstein-Leopoldshafen, Germany, (fax: +49 7247 808 666; e-mail: crysdata@fiz.karlsruhe.de) on quoting the depository number CSD_380413. The software Diamond [24] was utilized to create the graphic representation of the crystal structure with ellipsoidal representation (98% probability level) for all atoms.

Table 1
Selected crystallographic data and details of data collection for $Mn_{1.34}Sn_{6.66}Bi_8Se_{20}$.

Formula sum	$Mn_{1.34}Sn_{6.66}Bi_8Se_{20}$
Crystal system; space group	monoclinic; $C2/m$ (#12)
Formula weight (g/mol)	4115.13
Density (g/cm^3)	6.88
Lattice parameters (Å)	
$a=$	13.648(3)
$b=$	4.1745(8)
$c=$	17.463(4)
β (deg.)=	93.42(3)
Volume (Å^3); Z	993.2(3); 1
Crystal shape, color	Needle, black
Diffractometer	IPDS-2T (STOE)
Radiation/Å	$\lambda=0.7107$
φ range; Δφ (deg.); T(K)	180; 1.0; 299
$2\theta_{max}$(deg.);	58.2;
Index range	$-17 \le h \le 17$, $-5 \le k \le 5$, $-22 \le l \le 22$
Measured reflections	12529
Unique reflections	1505
R_{int}/R_σ	0.0493/0.0199
μ (cm^{-1})	581
N parameters	63
Extinction correction	0.00014(1)
Difference e$^-$ density (e/Å^3)	+0.98 to −1.00
R_1 ($F_o > 4\sigma(F_o)$)[a]	0.021
wR_2 (all)[b]	0.057
GooF	1.202

[a] $R_1 = \sum ||F_0|-|F_c|| / \sum |F_0|$
[b] $R_2 = [\sum w(F_0^2-F_c^2)^2 / \sum w(F_0^2)^2]^{1/2}$

Table 2
Wyckoff positions (W.P.), site occupancy factors (k), atomic coordinates, and equivalent isotropic displacement parameters ($U_{eq}/\times 10^{-4}$ Å^2) for all atoms in the asymmetric unit of $Mn_{1.34}Sn_{6.66}Bi_8Se_{20}$. Estimated standard deviations corresponding to the last digits are indicated in parenthesis.

Position	Atom	W. P.	k	x	y	z	U_{eq} [$\times 10^{-4}$ Å^2]
M(1)	Bi1	4*i*	0.52(2)	0.0378(2)	0	0.2806(1)	241(4)
	Sn1	4*i*	0.48(2)	0.0378(2)	0	0.2806(1)	241(4)
M(2)	Bi2	4*i*	0.57(2)	0.2340(2)	0	0.6159(2)	222(4)
	Sn2	4*i*	0.43(2)	0.2340(2)	0	0.6159(2)	222(4)
M(3)	Bi3	4*i*	0.70(2)	0.2890(2)	0	0.1082(2)	371(6)
	Sn3	4*i*	0.30(2)	0.2890(2)	0	0.1082(2)	371(6)
M(4)	Bi4	2*d*	0.41(2)	0	1/2	1/2	230(8)
	Sn4	2*d*	0.59(2)	0	1/2	1/2	230(8)
M(5)							
	Sn5	2*a*	0.33(2)	0	0	0	290(9)
	Mn	2*a*	0.67(2)	0	0	0	290(9)
Se(1)	Se1	4*i*		0.0680(3)	0	0.8627(2)	306(9)
Se(2)	Se2	4*i*		0.1331(2)	0	0.4472(2)	190(6)
Se(3)	Se3	4*i*		0.3974(2)	0	0.3409(2)	221(7)
Se(4)	Se4	4*i*		0.6416(2)	0	0.0344(2)	230(7)
Se(5)	Se5	4*i*		0.6677(2)	0	0.2391(2)	209(7)

U_{eq} is defined as one-third of the trace of the orthogonalized U_{ij} tensor

Table 3
Selected inter-atomic distances (Å) in $Mn_{1.34}Sn_{6.66}Bi_8Se_{20}$. Estimated standard deviations corresponding to the last digits are indicated in parenthesis.

Bond	Length (Å)	Bond	Length (Å)
M(1)—Se(1)^{i}	2.813(4)	M(2)—Se(5)^{iv}	2.794(4)
M(1)—Se(5)$^{ii,\ iii}$	2.860(2)	M(2)—Se(3)$^{v,\ vi}$	2.882(3)
M(1)—Se(3)$^{ii,\ iii}$	3.062(3)	M(2)—Se(2)$^{v,\ vi}$	3.016(3)
M(1)—Se(2)	3.115(4)	M(2)—Se(2)	3.177(4)
M(3)—Se(4)^{vii}	2.717(4)	M(4)—Se(2)	2.951(2)
M(3)—Se(1)$^{v,\ vi}$	2.882(3)	M(4)—Se(2)$^{i,\ viii,\ ix}$	2.951(2)
M(3)—Se(4)$^{ii,\ iii}$	3.123(3)	M(4)—Se(3)$^{ii,\ vi}$	3.035(3)
M(3)—Se(5)$^{ii,\ iii}$	3.574(3)		
M(5)—Se(1)^{i,x}	2.622(4)		
M(5)—Se(4) $^{ii,\ iii,\ xi,\ xii}$	2.883(2)		

Operators for generating equivalent atoms
(i) $-x, -y, 1-z$; (ii) $-0.5+x, 0.5+y, z$; (iii) $-0.5+x, -0.5+y, z$; (iv) $1-x, -y, -z$; (v) $0.5-x, -0.5-y, 1-z$; (vi) $0.5-x, 0.5-y, 1-z$; (vii) $1-x, -y, -z$; (viii) $x, 1+y, z$; (ix) $-x, 1-y, 1-z$; (x) $x, y, -1+z$; (xi) $0.5-x, -0.5-y, -z$; (xii).

2.2.3. Differential scanning calorimetry (DSC)

DSC analysis of the finely ground product was performed to assess melting and crystallization temperatures as well as the thermal stability of the compound. DSC data were recorded using approximately 10 mg of finely ground powder of the synthesized compound and an equivalent mass of alumina (Al_2O_3) as the reference. Both the sample and the reference, sealed in a small quartz tube under residual pressure of 10^{-4} Torr, were placed on the sample and reference pans in an F401 DSC apparatus (NETZSCH) maintained under flowing nitrogen gas. The sample and reference were simultaneously heated to 1073 K at a rate of 15 K/min, isothermed for 2 min and then cooled to 473 K at a rate of 15 K/min. DSC data were recorded during two heating and cooling cycles. The endothermic onset temperatures are reported as the melting points and the exothermic onset temperatures are crystallization points.

2.2.4. Magnetic susceptibility measurements

The magnetic susceptibility of $Mn_{1.34}Sn_{6.66}Bi_8Se_{20}$ was calculated from the magnetic moment measured as a function of

temperature using a Quantum Design MPMS-XL SQUID magnetometer. A polycrystalline powder sample of $Mn_{1.34}Sn_{6.66}Bi_8Se_{20}$ (~50 mg) was mounted inside a clear plastic straw sample holder, the magnetic moment contribution of which was subtracted from the combined (sample+sample holder) measurement. DC magnetic susceptibility measurements, field cooled (FC) and zero field cooled (ZFC), were performed over a temperature range 2–300 K and with an applied magnetic field of 100 Oe.

2.2.5. Infrared spectroscopy

Room temperature optical diffuse reflectance measurement was performed on finely ground powder of $Mn_{1.34}Sn_{6.66}Bi_8Se_{20}$ to probe the optical energy band gap. The spectrum was measured in the 4000–400 cm^{-1} region with a Thermo Nicolet NEXUS 670 FT-IR spectrometer equipped with a diffuse reflectance accessory from PIKE Technology Inc. Absorption (α/S) data were calculated from reflectance data using the Kubelka–Munk function [25–27] and the optical band gap was determined to be the intercept of the linearized baseline with the linearized absorption edge from the α/S versus E (eV) plot.

2.2.6. Thermal conductivity

The thermal diffusivity data of $Mn_{1.34}Sn_{6.66}Bi_8Se_{20}$ was recorded from room temperature to 575 K under flowing nitrogen gas using the flash diffusivity method on a LFA 457/2/G Microflash apparatus (NETZSCH). The front face of the graphite coated disc-shaped specimen ($\phi=13$ mm; thickness ~2.5 mm) was irradiated by a short laser burst, and the temperature rise of the rear face was recorded and analyzed. Thermal conductivity (κ) values were calculated using the equation $\kappa=\alpha C_p d$, where α is the thermal diffusivity, C_p the specific heat (extracted from the laser flash data using the C_p of pyroceram as reference) and d the density calculated from pellet geometry and mass. The lattice thermal conductivity ($\kappa_{lattice}$) of $Mn_{1.34}Sn_{6.66}Bi_8Se_{20}$ was obtained by subtracting the electronic contribution (calculated using the Wiedemann–Franz law, $\kappa_{elec}=\sigma LT$, $L=2.44\times10^{-8}$ WΩ/K^2) from the total thermal conductivity.

2.2.7. Charge transport measurements

Thermopower and electrical conductivity data for $Mn_{1.34}Sn_{6.66}Bi_8Se_{20}$ were measured simultaneously using a commercial ZEM-3 Seebeck coefficient/electrical resistivity measurement system (ULVAC-RIKO, Japan). Data were recorded in the temperature range from 300 to 575 K using a rectangular bar specimen, with approximate dimensions $2.5\times2.5\times10$ mm^3, cut from an approximately 96% dense hot pressed pellet of $Mn_{1.34}Sn_{6.66}Bi_8Se_{20}$. To ensure reproducibility, data were collected on three heating and cooling cycles under a residual pressure of He gas.

3. Results and discussion

3.1. Crystal structure

The quaternary manganese tin bismuth selenide $Mn_{1.34}Sn_{6.66}Bi_8Se_{20}$ crystallizes with the $AgBi_3S_5$ [11] (pavonite) and is the second (along with $MnSn_3Bi_8Se_{16}$) quaternary Mn-bearing bismuth selenide belonging to the pavonite homologous series. In the crystal structure (Fig. 2A), two types of building modules, denoted A and B, alternate along [0 0 1]. In module A, paired rods of face-sharing monocapped trigonal prisms alternate along the a-axis with a single chain of edge-sharing octahedra. In the structure of $AgBi_3S_5$, the monocapped trigonal prism is exclusively occupied by Bi, while the octahedral position is filled by Ag. From the structure refinement of $Mn_{1.34}Sn_{6.66}Bi_8Se_{20}$

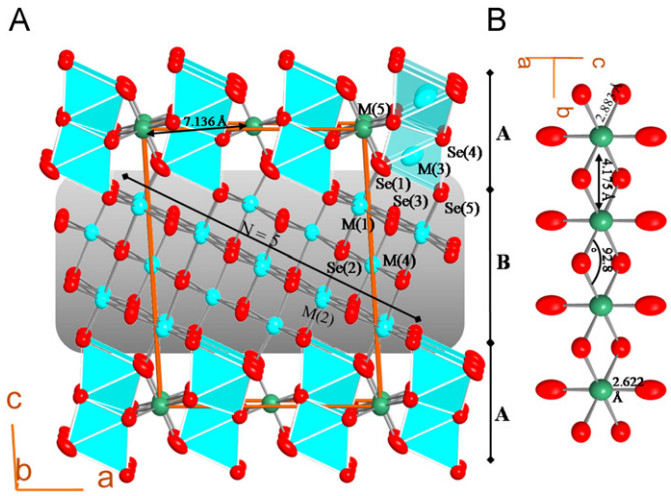

Fig. 2. (A) Crystal structure of $Mn_{1.34}Sn_{6.66}Bi_8Se_{20}$ projected along [0 1 0]. The two types of layered building units alternating along [0 0 1] are indicated. Polyhedra show paired rods of monocapped trigonal prisms around the M(3) position. The number of metal sites within module B, which indicates to the order number ($N=5$) in the pavonite homologous series is highlighted by the diagonal black line. (B) Geometric details of the {(Mn/Sn)Se_6} magnetic chain of edge-sharing octahedra within module A. Ellipsoids correspond to 98% probability level.

the sevenfold position, M(3), is mixed between Bi and Sn with strong preference for Bi (Bi/Sn: 70%/30%), while the octahedral metal position, M(5), is occupied by Mn and Sn in a 2:1 ratio. The M(5) position, which is the only position containing Mn atoms, forms a quasi-one-dimensional single chain of edge-sharing {(Mn/Sn)Se_6} octahedra (running along [0 1 0]) in which one of every three atoms is the diamagnetic Sn^{2+}.

Module B is composed of chains of edge-sharing [(Bi/Sn)Se_6] octahedra forming an NaCl-type fragment. The thickness of building unit B is defined by the number of metal sites along the [0 1-1] direction of the NaCl lattice (central diagonal of module B). This building unit (module B) in the structure of $Mn_{1.34}Sn_{6.66}Bi_8Se_{20}$ contains five metal positions along its central diagonal (Fig. 2A) and therefore, can be described as a new quaternary member of the pavonite homologous series with $N=5$, which is also referred to as ^{5}P according to the nomenclature of pavonite homologues [11]. All metal positions within module B are mixed occupied by Bi and Sn, with Sn showing preference for the metal site M(4) at the center (Sn/Bi: 59%/41%). Conversely, Bi is more abundant at the metal sites at the interface between modules B and A (Table 2). A similar distribution of Sn and Bi in metal sites within the NaCl-type building unit was reported in the structures of $MnSn_3Bi_8Se_{16}$ [10], $InSn_2Bi_3Se_8$ [28], $In_{0.2}Sn_6Bi_{1.8}Se_9$ [28], $KSn_5Bi_5Se_{13}$ [29], $K_xSn_{6-2x}Bi_{2+x}Se_9$ [29], $K_{1-x}Sn_{5-x}Bi_{11+x}Se_{22}$ [30] and $A_{1-x}Sn_{3-x}Bi_{11+x}Se_{20}$ [31].

An examination of the coordination environment of metal sites within module B revealed nearly ideal octahedral coordination for M(4) site located at the center of the layer with bond distances between 2.951(2) and 3.035(3) Å, while the octahedral environment of M(1) and M(2) sites located at the border of module B are distorted towards a [1+2+2+1] geometry, suggesting that the lone pairs of Bi^{3+} and Sn^{2+} are expressed at the periphery. The M(3) site, located in the monocapped trigonal prismatic coordination within module A, is shifted towards one of the faces of the prism as indicated by the strong interaction with the Se(4) atom (2.717(4) Å) capping one face of the trigonal prism, while the remaining edges are more remote with M(3)–Se distances of 2.882(3) Å; 3.123(3) Å and 3.574(3) Å (Table 3). These bond distances are comparable to values found in other multinary

selenides containing mixed-site occupancies between Bi and Sn, such as $MnSn_3Bi_8Se_{16}$ [10], $InSn_2Bi_3Se_8$ [28], $In_{0.2}Sn_6Bi_{1.8}Se_9$ [28], $KSn_5Bi_5Se_{13}$ [29], $K_xSn_{6-2x}Bi_{2+x}Se_9$ [29], $K_{1-x}Sn_{5-x}Bi_{11+x}Se_{22}$ [30] and $A_{1-x}Sn_{3-x}Bi_{11+x}Se_{20}$ [31]. The metal position M(5) located within module A shows a strongly distorted octahedral environment (towards [2+4] geometry) with four long equatorial bonds at 2.883(2) Å, and two short apical bonds at 2.622(2) Å.

3.1.1. Perspective of the new family of quaternary manganese-bearing bismuth selenides

The observed distribution of atoms within metal sites in the structures of $MnSn_3Bi_8Se_{16}$ [10] and $Mn_{1.34}Sn_{6.66}Bi_8Se_{20}$, (nothing that the octahedral metal position within module A is exclusively mixed occupied by Mn and Sn, while the remaining metal sites are mixed occupied by Bi and Sn), strongly suggests the existence of a large family of quaternary compounds with pavonite structures in the Mn –Sn–Bi–Se system. This new atomic distribution in $MnSn_3Bi_8Se_{16}$ [10] and $Mn_{1.34}Sn_{6.66}Bi_8Se_{20}$, and the resulting final compositions obtained from structure refinements can be summarized by the general formula, $Mn_tSn_{1-t+y}Bi_{[6+2(N+1-y)]/3}Q_{N+5}$ ($Z=2$), where t is the degree of substitution of Sn by Mn in the octahedral position within module A ($0 \le t \le 1$); y the degree of substitution of Bi by Sn in the remaining metal sites in the structure ($0 \le y \le N+1$); and N the number of metal sites along the central diagonal of module B ($N \ge 0$). The compositions $MnSn_3Bi_8Se_{16}$ and $Mn_{1.34}Sn_{6.66}Bi_8Se_{20}$ are the first members of this broad family of compounds with {$t=0.5$; $y=1$; $N=3$} and {$t=0.67$; $y=3$; $N=5$}, respectively. By adjusting the compositional and structural parameters t, y and/or N, a large number of compounds with different compositions and closely related structures can be generated. Within a given structure type (constant N), for example, $Mn_tSn_{1-t+y}Bi_{[6+2(6-y)]/3}Se_{10}$ ($N=5$), the variation of t, and y will result in several isostructural compositions with tunable electronic and magnetic properties. For $t=1$, a full quasi-one-dimensional chain of magnetic atoms {$MnSe_6$} running along the b-axis (Fig. 2B) is expected. The electronic properties within $MnSn_yBi_{[6+2(6-y)]/3}Se_{10}$ ($t=1$, $N=5$) isostructural phases can also be tuned by adjusting the compositional parameter y. This structural and compositional flexibility in the $Mn_tSn_{1-t+y}Bi_{[6+2(N+1-y)]/3}Q_{N+5}$ family of compounds points to the accessibility of many interesting electronic and magnetic properties. Investigations of the structure/composition/properties relationships of several members of this family as well as the Fe analogs are in progress.

3.1.2. Magnetism and structure–composition–magnetism relationship

The molar magnetic susceptibility as well as the inverse susceptibility of $Mn_{1.34}Sn_{6.66}Bi_8Se_{20}$ measured in the temperature range from 2 to 300 K is shown in Fig. 3. The compound follows Curie–Weiss law, $1/\chi_M=(T-\theta_p)/C$, between 50 and 300 K. The observed effective magnetic moment, $\mu_{eff} \approx 5.5\,\mu_B$ (calculated from FC data) per Mn ion, although slightly smaller than the theoretical μ_{eff} of 5.92 μ_B for Mn^{2+} (d^5) in high spin, is in agreement with the assignment of the oxidation state of Mn ions (2+) in the crystal structure. The magnetic susceptibility curves (FC and ZFC) showed a maximum at $T_N=10$ K, which presumably corresponds to a spin glass or an antiferromagnetic transition as revealed by the negative Curie paramagnetic temperatures of $\theta_p=-14$ K and $\theta_p=-3$ K observed for FC and ZFC data, respectively. Above the transition temperature, the susceptibility is independent of field, while a slight divergence can be observed in ZFC and FC data below $T_N=10$ K. The weak amplitude of the maximum observed on the susceptibility curves probably results from the dilution within the quasi-one-dimensional {Mn/Sn)Se_6} magnetic single chain (Fig. 2B), where one

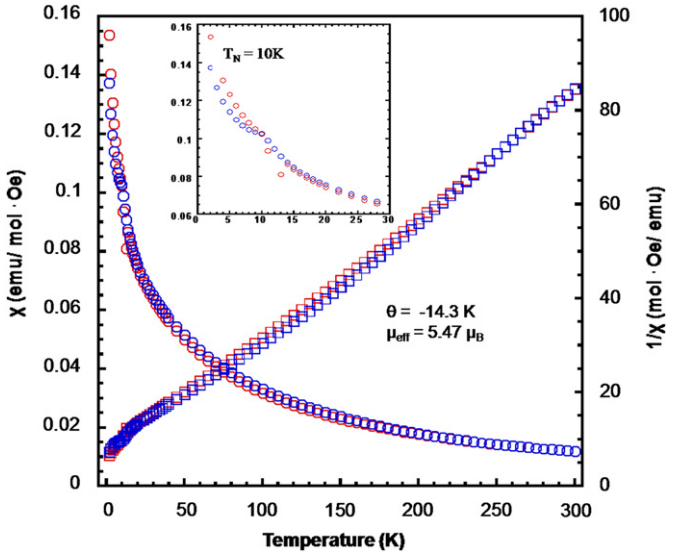

Fig. 3. Temperature dependence of the magnetic susceptibility (χ) and inverse susceptibility ($1/\chi$) of $Mn_{1.34}Sn_{6.66}Bi_8Se_{20}$ measured in an applied magnetic field of 100 Oe (FC: red symbols; ZFC: blue symbols).(For interpretation of the references to color in this figure legend, the reader is referred to the web version of this article.)

out of every three (33%) atoms along the b-axis is Sn rather than Mn.

The observed antiferromagnetic behavior of $Mn_{1.34}Sn_{6.66}Bi_8Se_{20}$ can be understood in the light of Goodenough–Kanamori rules [32–34] through careful examination of the structural geometry of the magnetic chain. {Mn/Sn)Se_6} magnetic single chains in $Mn_{1.34}Sn_{6.66}Bi_8Se_{20}$ are well isolated with inter-chain distances of 7.136(2) Å along the a-axis and 17.463(4) Å along the c-axis. Therefore, magnetic interactions between adjacent chains are negligible and the magnetic behavior of the compound is controlled by the intra-chain exchange interactions between neighboring magnetic atoms (along b-axis). As can been seen in Fig. 2B, the distance of 4.175(2) between adjacent Mn/Sn atoms along the b-axis is too long for direct exchange interactions and the observed magnetic ordering presumably results from indirect exchange interactions through the Se atom bridging adjacent Mn/Sn atoms. According to the Goodenough–Kanamori rules, the observed (Mn/Sn)–Se–(Mn/Sn) bond angle of 92.8(4)° suggests weak antiferromagnetic interaction between adjacent magnetic centers, which is consistent with the experimental data (Fig. 3).

3.1.3. Thermoelectric properties

Fig. 4A shows the electrical conductivity and thermopower of $Mn_{1.34}Sn_{6.66}Bi_8Se_{20}$. The compound is a semiconductor with the electrical conductivity increasing with rising temperature. The Arrhenius plot of the electrical conductivity results in an activation energy of ~0.34 eV. At 300 K, the electrical conductivity value is ~47 S/cm and increases monotonically to 91 S/cm at 575 K. The observed room temperature value of the electrical conductivity is comparable to values reported for $InSn_2Bi_3Se_8$ ($\sigma \approx 78.59$ S/cm), $In_{0.2}Sn_6Bi_{1.8}Se_9$ ($\sigma \approx 19.74$ S/cm) [26], but is lower than values of 133 S/cm and 650 S/cm obtained for $MnSn_3Bi_8Se_{16}$ [10] and the optimized $K_xSn_{6-2x}Bi_{2+x}Se_9$ system [29], respectively. $Mn_{1.34}Sn_{6.66}Bi_8Se_{20}$ showed negative thermopower values in the measured temperature range 300–575 K indicating n-type semiconducting behavior with electrons as the dominant charge carriers (Fig. 4A). As the temperature increases the thermopower decreases from −123 μV/K at 300 K to −90 μV/K at 575 K. The thermopower of $Mn_{1.34}Sn_{6.66}Bi_8Se_{20}$ at room temperature (−123 μV/K) is slightly larger than the value observed for the

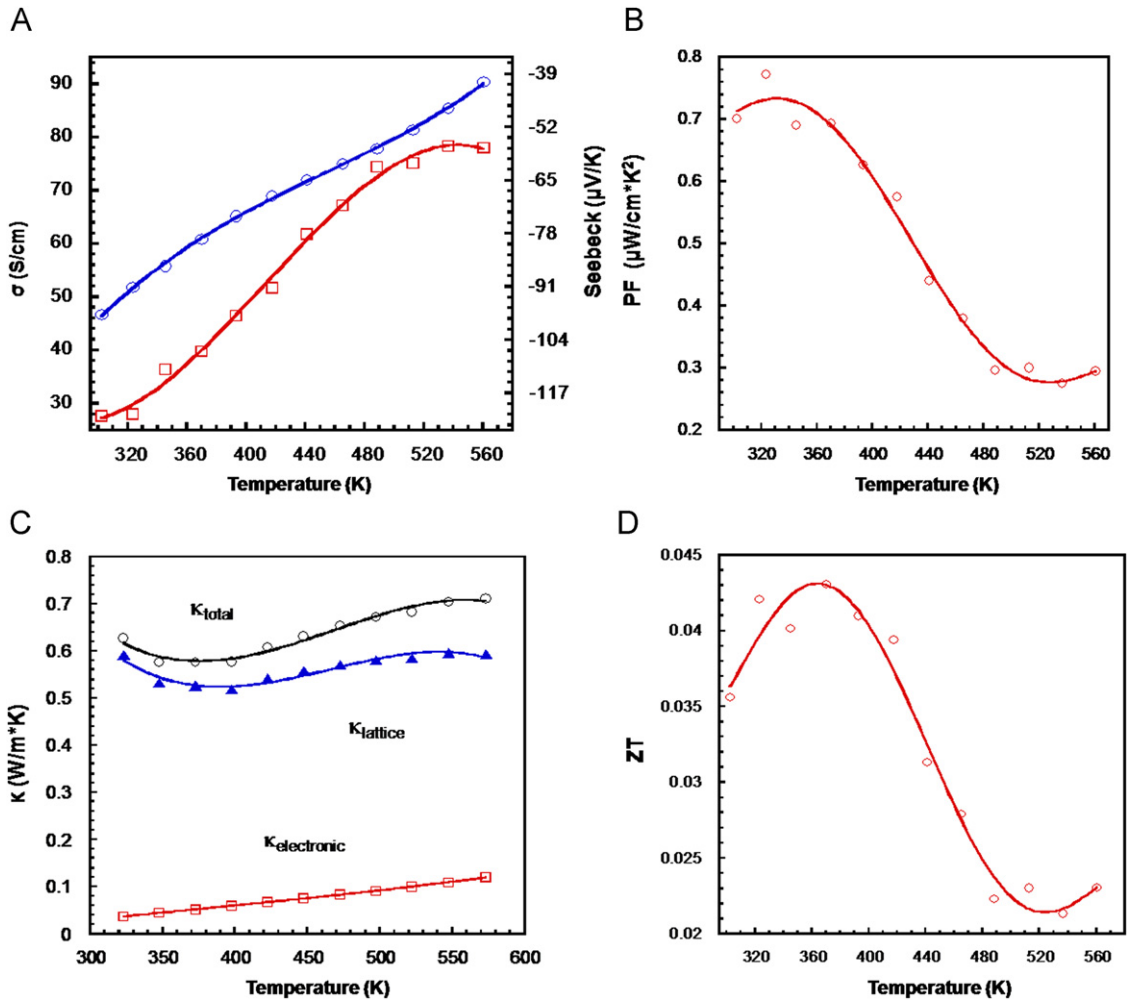

Fig. 4. Temperature dependence of the thermoelectric properties of $Mn_{1.34}Sn_{6.66}Bi_8Se_{20}$: (A) electrical conductivity (σ) and thermopower (S); (B) power factor; (C) total thermal conductivity (κ) along with the lattice and electronic contributions; (D) calculated figure of merit (ZT). All lines are to guide the eye and do not represent a theoretical fit to the data.

$MnSn_3Bi_8Se_{16}$ homologue ($-97\,\mu V/K$) [10] and almost three times that of $K_xSn_{6-2x}Bi_{2+x}Se_9$ ($-48\,\mu V/K$) [29]. However, it is considerably lower than the values of -270 and $-230\,\mu V/K$ reported for $InSn_2Bi_3Se_8$ and $In_{0.2}Sn_6Bi_{1.8}Se_9$, respectively [28]. The low electrical conductivity and the thermopower of $Mn_{1.34}Sn_{6.66}Bi_8Se_{20}$ results in a maximum power factor ($\sigma.S^2$) value of $0.7\,\mu W/cm\,K^2$ at 325 K (Fig. 4B).

The thermal conductivity was measured between 300 and 575 K on a hot pressed pellet of $Mn_{1.34}Sn_{6.66}Bi_8Se_{20}$. The total thermal conductivity along with the lattice and the electronic contributions are shown in Fig. 4C. The total thermal conductivity is $\sim$0.63 W/m K at 300 K and increased to $\sim$0.7 W/m K at 575 K after reaching a minimum value of $\sim$0.58 W/m K at 375 K. Because of the low electrical conductivity of $Mn_{1.34}Sn_{6.66}Bi_8Se_{20}$, the observed total thermal conductivity derives essentially from the lattice contribution. The lattice thermal conductivity decreases from 0.6 W/m K at 300 K to 0.5 W/m K at 400 K and increases slightly thereafter. The observed value of the lattice thermal conductivity of $Mn_{1.34}Sn_{6.66}Bi_8Se_{20}$ is one-third to one-fourth the values reported for state-of-the-art Bi_2Te_3 bulk, thin film and superlattice thermoelectric materials [35–37] and about twice that of (BiSbTe) nanocomposite materials [38]. Such a low value for the lattice thermal conductivity can be attributed to the combination of low crystal symmetry and complex chemical composition, with heavy elements such as Sn and Bi, in $Mn_{1.34}Sn_{6.66}Bi_8Se_{20}$.

The thermoelectric figure of merit (ZT) of $Mn_{1.34}Sn_{6.66}Bi_8Se_{20}$ is shown in Fig. 4D. The ZT increases with rising temperature from $\sim$0.035 at 300 K to a maximum value of 0.043 at $\sim$370 K, then decreases to a minimum value of 0.02 at $\sim$490 K with a further increase in temperature. Although the observed figure of merit of $Mn_{1.34}Sn_{6.66}Bi_8Se_{20}$ is low for thermoelectric applications, the incredibly low lattice thermal conductivity observed makes this composition attractive for further exploration aiming at optimizing the power factor. The electrical conductivity and thermopower can be enhanced without significant increases in the total thermal conductivity by varying the Sn/Bi ratio (varying y) according to the general formula $Mn_tSn_{1-t+y}Bi_{[6+2(6-y)]/3}Se_{10}$ or by partial Te doping on Se sites in the structure.

3.1.4. Energy gap and thermal analysis

The diffuse reflectance infrared absorption spectrum of $Mn_{1.34}Sn_{6.66}Bi_8Se_{20}$ was recorded at room temperature in the range 0.05–0.5 eV. The band gap estimated from the (α/S) versus energy plot is about 0.29 eV indicating again that $Mn_{1.34}Sn_{6.66}Bi_8Se_{20}$ is a narrow gap semiconductor (Fig. 5A). The observed value of the energy gap is consistent with the black color of the crystals as well as the measured charge transport properties.

The thermal behavior of $Mn_{1.34}Sn_{6.66}Bi_8Se_{20}$ was investigated by differential scanning calorimetry (DSC). The compound melts

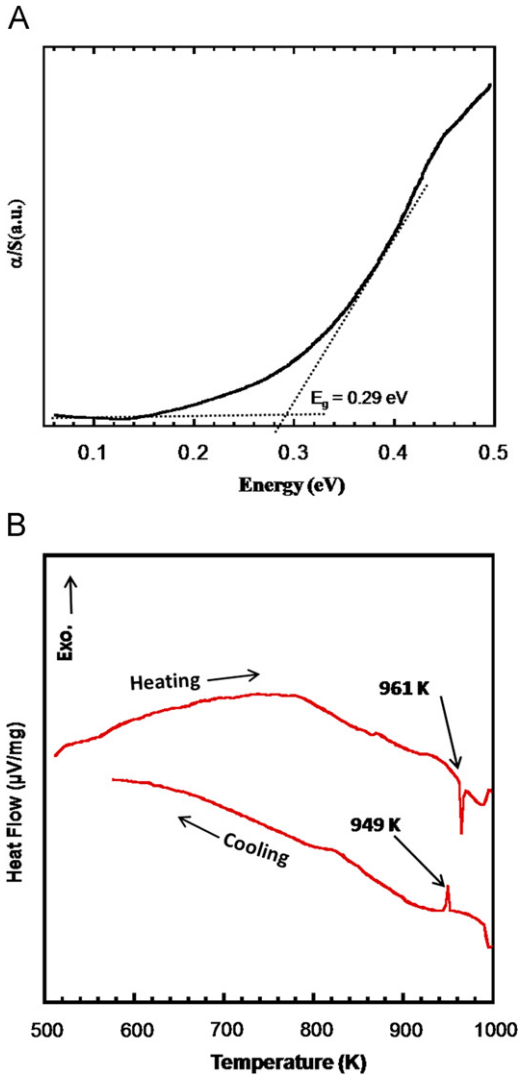

Fig. 5. (A) Optical absorption spectrum of $Mn_{1.34}Sn_{6.66}Bi_8Se_{20}$ measured at room temperature showing the energy band gap. (B) Differential scanning calorimetry (DSC) plots for $Mn_{1.34}Sn_{6.66}Bi_8Se_{20}$ showing endothermic peak corresponding to congruent melting upon heating and the crystallization peak upon cooling.

congruently at 961 K and crystallizes at 949 K on cooling (Fig. 5B). The thermal stability of the compound was also confirmed by repeating heating and cooling cycles.

4. Conclusion

$Mn_{1.34}Sn_{6.66}Bi_8Se_{20}$, a new quaternary mixed metal selenide in the Mn/Sn/Bi/Se system was synthesized as nearly single phase via solid state reaction of the elements at 723 K. X-ray single crystal structure determination indicated that $Mn_{1.34}Sn_{6.66}Bi_8Se_{20}$ is a new member of the pavonite homologous series with $N=5$. $Mn_{1.34}Sn_{6.66}Bi_8Se_{20}$ undergoes a weak antiferromagnetic transition at $T_N=10$ K. Above 10 K, the magnetic susceptibility obeys the Curie–Weiss law and the estimated effective magnetic moment $\mu_{eff} \approx 5.5\,\mu_B$ per Mn ion, is in agreement with the assignment of the oxidation state of Mn ions (2+) in the crystal structure. Optical absorption spectroscopy and charge transport measurements revealed that $Mn_{1.34}Sn_{6.66}Bi_8Se_{20}$ is a narrow gap n-type semiconductor with very low lattice thermal conductivity of about 0.6W/m K at 300 K. The compound melts congruently and is thermally stable up to 1073 K.

Acknowledgments

This work was partially supported by the National Science Foundation Career Award (DMR-0954817), the Louisiana Board of Regents (Grant # NSF(2008)-PFUND-126) and the University of New Orleans Office of Research and Sponsored Programs (SCoRe2009 award and start-up funds). This work made use of the laser flash diffusivity apparatus (LFA4-57) purchased with funds from the Louisiana Board of Regents (Grant # LEQSF(2008-09)-ENH-TR-58).

Appendix A. Supplementary data

Supplementary data associated with this article can be found in the online version at doi:10.1016/j.jssc.2010.04.035

References

[1] P. Leone, C. Doussier, G. Andre, Y. Moelo, Phys. Chem. Minerals 35 (2008) 201–206.
[2] M. Winterberger, G. Andre, Physica B 162 (1990) 5–12.
[3] P. Leone, L.-M. Le Leuch, P. Palvadeau, P. Molinie, Y. Meolo, Solid State Sci. 5 (2003) 771–776.
[4] Y. Matsushita, Y. Ueda, Inorg. Chem. 42 (2003) 7830–7838.
[5] S. Derakhshan, A. Assoud, N. Soheilnia, H. Kleinke, J. Alloys Compd. 390 (2005) 51–54.
[6] P. Leone, G. Andre, C. Doussier, Y. Moelo, J. Magn. Magn. Mater. 284 (2004) 92–96.
[7] S. Morimoto, Y. Matsushita, Y. Ueda, M. Kawase, T. Saito, S. Nakamura, S. Nasu, J. Magn. Magn. Mater. 284 (2007) e962–e964.
[8] S. Derakhshan, A. Assoud, N. Soheilnia, H. Kleinke, J. Alloys Compd. 390 (2005) 51–54.
[9] P.F.P. Poudeu, N. Takas, C. Anglin, J. Eastwood, A. Rivera, J. Am. Chem. Soc. 132 (2010) 5751–5760.
[10] C. Anglin, N. Takas, B. Giroire, C. Obiako, P. F. P. Poudeu, Inorg. Chem. (2010) submitted for publication.
[11] E. Makovicky, W.G. Mumme, J.A. Watts, Can. Mineral. 15 (1977) 339.
[12] Y. Takeuchi, J. Takagi, T. Yamanaka, Proc. Jpn. Acad. 50 (1974) 317.
[13] M. Ohmasa, W. Nowacki, Z. Kristallogr. 137 (1973) 422.
[14] M. Ohmasa, N. Jb. Miner. Mh. (1973) 227.
[15] W.G. Mumme, N. Jb. Miner. Mh. (1990) 193.
[16] H.K. Herbert, W.G. Mumme, N. Jb. Miner. Mh. (1981) 69.
[17] P.F.P. Poudeu, M. Ruck, Acta Cryst. C 61 (2005) i41–i43.
[18] E. Makovicky, Eur. J. Mineral. 5 (1993) 545–591.
[19] E. Makovicky, Rev. Mineral. Geochem. 6 (2006) 7–125.
[20] K.-B. Chen, C.-S. Lee, Solid State Sci. 11 (2009) 1666–1672.
[21] W. Kraus, G. Nolze, PowderCell for Windows Version 2.3; Federal Institute for Materials Research and Testing, Berlin, Germany, 1999.
[22] STOE X-area. Version 1.52. Stoe and Cie GmbH, Darmstadt, Germany, 2009.
[23] G. M. Sheldrick, SHELXTL DOS/Windows/NT Version 6.12; Bruker Analytical X-ray Instruments, Inc.: Madison, WI, 2000.
[24] K. Brandenburg, DIAMOND. Version 3.1a. Crystal Impact GbR, Bonn, Germany, 2005.
[25] W.W. Wendlandt, H.G. Hecht, Reflectance Spectroscopy, Interscience Publishers, New York, 1966.
[26] G. Kotuem, Reflectance Spectroscopy, Springer-Verlag, New York, 1969.
[27] S.P. Tandon, J.P. Gupta, Status Solidi 38 (1970) 363.
[28] M.-F. Wang, S.-M. Jang, J.-C. Huang, C.-S. Lee, J. Solid State Chem. 182 (2009) 1450–1456.
[29] A. Mrotzek, M.G. Kanatzidis, Inorg. Chem. 42 (2003) 7200–7206.
[30] A. Mrotzek, D.-Y. Chung, T. Hogan, M.G. Kanatzidis, J. Mater. Chem. 10 (2000) 1667–1672.
[31] M.G. Kanatzidis, Acc. Chem. Res. 38 (2005) 359–368.
[32] J. Goodenough, J. Phys. Chem. Solids 6 (1958) 287–297.
[33] J. Goodenough, Phys. Rev. 100 (1955) 564–573.
[34] J. Kanamori, J. Phys. Chem. Solids 10 (1959) 87–98.
[35] N. Peranio, O. Eibl, J. Nurnus, J. Appl. Phys. 100 (2006) 114306.
[36] X.A. Fan, J.Y. Yang, W. Zhu, S.Q. Bao, X.K. Duan, C.J. Xiao, Q.Q. Zhang, Z. Xie, J. Phys. D: Appl. Phys. 39 (2006) 5069–5073.
[37] I. Yamasaki, R. Yamanaka, M. Mikami, H. Sonobe, Y. Mori, T. Sasaki, in: Proceedings of the 17th International Conference on Thermoelectrics, 1998, pp. 210–213.
[38] B. Poudel, Q. Hao, Y. Ma, et al., Science 320 (2008) 634–638.